Available online at www.sciencedirect.com
ScienceDirect
Trans. Nonferrous Met. Soc. China 33(2023) 668−682

Transactions of
Nonferrous Metals
Society of China
www.tnmsc.cn

Effects of Zr/(Sc+Zr) microalloying on dynamic recrystallization, dislocation density and hot workability of Al−Mg alloys during hot compression deformation

Ying DENG[1,2], Xin-wen ZHU[1], Yi LAI[1], Yi-fan GUO[1], Le FU[1,3], Guo-fu XU[1,2], Ji-wu HUANG[1,2]

1. School of Materials Science and Engineering, Central South University, Changsha 410083, China;
2. Key Laboratory of Nonferrous Metal Materials Science and Engineering of Hunan Province,
Central South University, Changsha 410083, China;
3. Applied Materials Science, Department of Engineering Science, Uppsala University, Uppsala 75121, Sweden

Received 8 October 2021; accepted 4 March 2022

Abstract: The deformation behavior and microstructure characteristics of Al−6.00Mg, Al−6.00Mg−0.10Zr and Al−6.00Mg−0.25Sc−0.10Zr (wt.%) alloys were investigated by hot compression tests and electron microscopy methods. The results show that after deforming under the maximum processing efficiency condition (673 K, 0.01 s^{-1}), dislocation densities of Al−6.00Mg, Al−6.00Mg−0.10Zr and Al−6.00Mg−0.25Sc−0.10Zr alloys are 2.68×10^{16}, 8.93×10^{16} and 6.1×10^{17} m^{-2}, respectively. Their dynamic recrystallization fractions are 19.8%, 15.0% and 12.7%, respectively. Kernel average misorientation (KAM) analyses indicate that dislocation accumulation near grain boundaries is enhanced by adding Zr or Sc+Zr. Besides, the established hot processing maps, based on the dynamic material model (DMM), reveal that the addition of Zr or Sc+Zr can reduce the range of low-temperature unstable domain but expand the unstable domain at high temperatures and high strains. The experimental results further verify that under the testing deformation condition, only the Al−6.00Mg−0.25Sc−0.10Zr alloy cracks at 773 K and 1 s^{-1}.

Key words: Al−Mg alloys; Sc; Zr; hot deformation; dislocation density; dynamic recrystallization

1 Introduction

5xxx series (Al−Mg) aluminum alloys have been widely used in aerospace and shipbuilding industries due to their good mechanical properties and excellent corrosion resistance [1−4]. With the rapid development of industry technology, how to further improve the performance of existing aluminum alloys has become the focus of current research. The combined addition of Sc and Zr elements in aluminum alloys as strengthening elements has become a hot spot in the current research on aluminum alloys [5−8]. The addition of Sc and Zr to the aluminum alloy by microalloying technology can inhibit recrystallization process and increase the strength of the alloy. However, it is found that Al−Mg alloys containing microalloying elements are more prone to cracking during hot deformation through previous experimental research. Therefore, it is necessary to investigate the deformation behavior and mechanism of Al−Mg alloys with microalloying elements under different hot deformation conditions.

Dynamic material model (DMM) can establish the relationship among constitutive behavior, microstructure and hot workability [9]. The processing map can be used to investigate the effects of deformation temperatures and strain rates on flow behavior [10]. Previous studies further

---

Corresponding author: Ying DENG, Tel: +86-15974183275, E-mail: csudengying@163.com;

DOI: 10.1016/S1003-6326(22)66137-5

showed that the stable flow area in the processing map with high power dissipation efficiency was related to dynamic recrystallization (DRX) [11,12]. Therefore, the evolution of the microstructure under different deformation conditions can be predicted through the processing map. Meanwhile the processing map can also reflect the machinability of the studied alloy, and thus, the best hot deformation parameters of the alloy can be obtained by examining the processing map. For instance, ZANG et al [13] studied the hot deformation behavior and the processing map of an Al−7.9Zn−2.7Mg−2.0Cu alloy. They found that the best thermal deformation range was as follows: a deformation temperature range of 400−450 °C, a strain range of 0.005 s^{-1}, and a peak efficiency of 38%. Many studies focused on DRX behavior under different deformation temperatures and strain rates. LIN et al [14] found that the proportion of dynamic recrystallization (DRX) and low dislocation density regions were higher in the optimum hot deformation region than in the instability region.

The main purpose of this study is to investigate the hot deformation behavior of Al−Mg alloys without and with Zr or Sc+Zr. In order to optimize the hot deformation processing conditions, the processing maps will be established. Based on the above results, the influence of the addition of Zr or Sc+Zr on the hot workability of Al−Mg alloys will be clarified.

2 Experimental

The experimental materials of Al−Mg, Al−6.00Mg−0.10Zr and Al−6.00Mg−0.25Sc−0.10Zr (wt.%) alloys were homogenized. Their chemical compositions were listed in Table 1. The three alloys were processed into cylinders with a diameter of 10 mm and a height of 15 mm. The initial microstructures of the three alloys before deformation were shown in Fig. 1. It can be found that the three alloys were composed of equiaxed grains, and the average grain size of Al−Mg, Al−Mg−Zr and Al−Mg−Sc−Zr alloys is 132, 87 and 48 μm, respectively.

Isothermal compression tests were carried out on a Gleeble−3500 at five different temperatures (573,623, 673, 723, and 773 K) and four different strain rates (0.001, 0.01, 0.1, and 1 s^{-1}). Before the compression, the samples were heated to the

Table 1 Compositions of three alloys (wt.%)

Alloy	Mg	Si+Fe	Cu	Mn	Sc	Zr	Al
Al−Mg	5.98	0.75	0.10	0.47	−	−	Bal.
Al−Mg−Zr	6.00	0.70	0.10	0.40	−	0.10	Bal.
Al−Mg−Sc−Zr	6.01	0.68	0.10	0.45	0.25	0.10	Bal.

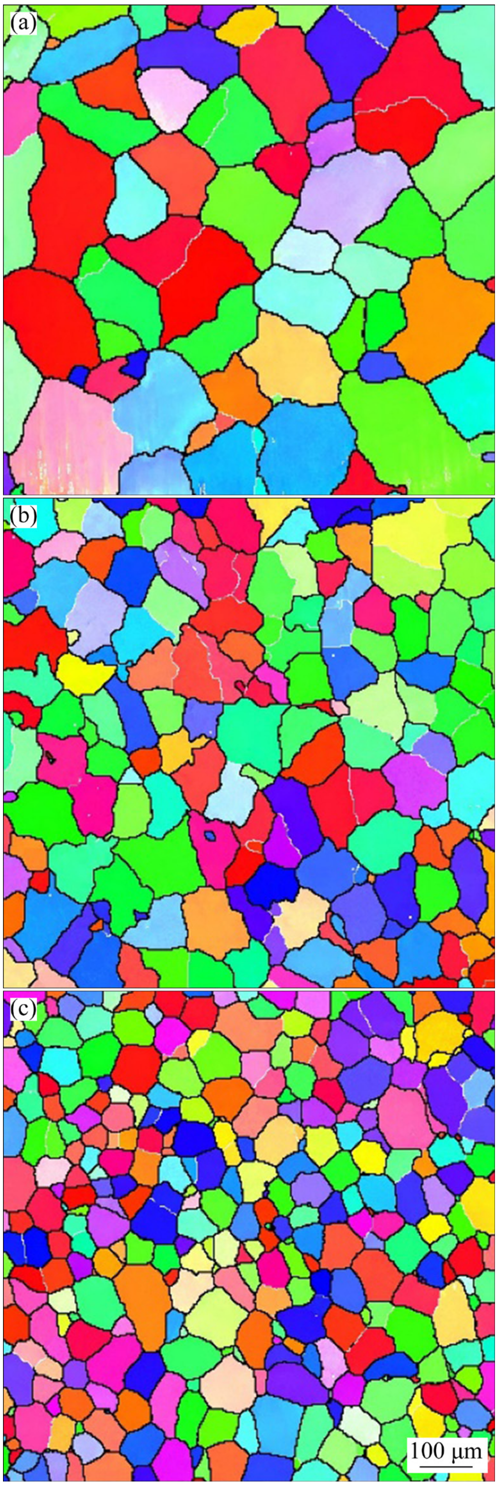

Fig. 1 IPF maps of three homogenized alloys: (a) Al−6.00Mg; (b) Al−6.00Mg−0.10Zr; (c) Al−6.00Mg−0.25Sc−0.10Zr

designed temperatures for 180 s with a heating rate of 3 K/s. All samples were compressed to a total true strain of 0.9 and then quenched into water immediately.

The phase composition of the studied alloy was examined on a Rigaku−2500 X-ray diffraction (XRD) with a scanning speed of 2 (°)/min. The XRD results were analyzed by a Jade 6.5 software and the full width at half maximum (FWHM) was corrected by deducting the FWHM from the XRD instrument. The microstructures of the studied alloys were studied by XRD and electron back-scattered diffraction (EBSD). The samples for EBSD observation were mechanically polished and electropolished in a solution of $V(\mathrm{HNO_3}):V(\mathrm{CH_3OH})=1:3$ at a temperature of 253 K. The specimens were characterized on an FEI Helios nano-lab 600i scanning electron microscope (SEM) equipped with an EBSD detector (Oxford, NordlysMax2), with an accelerating voltage of 20 kV and a step size of 2.5 μm.

3 Results

3.1 Stress−strain behavior and friction correction of flow stress

True stress−strain curves of the three studied alloys deformed under different conditions are shown in Fig. 2. Flow stress of the three alloys shows initial work hardening, followed by steady state and/or flow softening stage, depending on the deformation strain rate and temperature. After deforming at low temperatures and low strain rates, such as 573 K, 0.001 $\mathrm{s^{-1}}$ and 673 K, 0.001 $\mathrm{s^{-1}}$, the flow stress reaches the peak flow stress firstly, and then gradually decreases, which indicates the occurrence of flow softening. When the strain rate is high (1 $\mathrm{s^{-1}}$) and the temperature is low (573 K), the stress monotonously increases during the whole deformation process. This indicates that dynamic softening of the alloys is limited. It is worth noting that the peak flow stress and steady-state flow stress of the Al−Mg alloy with the addition of Zr or Sc+Zr are higher than those of the Al−Mg alloy.

During hot compression, the friction between the samples and the device plays an important role. This is because the friction can increase the flow stress during deformation. Therefore, the experimental flow stress needs to be corrected. EBRAHIMI and NAJAFIIADEH [15] proposed a method to quantitatively estimate the friction coefficient. The basic equation is as follows [15,16]:

$$\frac{p}{\sigma}=\frac{8b_1R}{H}\cdot\left\{\left[\frac{1}{2}+\left(\frac{H}{Rb_1}\right)^2\right]^{3/2}-\left(\frac{H}{Rb_1}\right)^3-\frac{m_1\mathrm{e}^{-b_1/2}}{24\sqrt{3}(\mathrm{e}^{-b_1/2}-1)}\right\} \tag{1}$$

where p is the uncorrected external pressure (measured pressure) applied to the sample after compression, σ is the true stress after correction, m is the constant friction coefficient in the compression test, b_1 is the barrel parameter, and R and H are the radius and height of the sample in the process of compression, respectively. In the equation, $R=R_0\exp(-\varepsilon/2)$, $H=h_0\exp(-\varepsilon)$, where R_0 and h_0 are the initial radius and height of the sample, respectively, and ε is the strain. m_1 and b_1 are determined by the following equations:

$$m_1=\frac{R_\mathrm{f}}{h}\cdot\frac{3\sqrt{3}b_1}{12-2b_1} \tag{2}$$

$$b_1=4\frac{R_\mathrm{M}-R_\mathrm{T}}{R_\mathrm{f}}\cdot\frac{h_1}{h_0-h_1} \tag{3}$$

where R_f is the average radius of the deformed sample, R_T is the top radius of the deformed sample, h_1 is the height of the deformed sample, and R_M is the maximum radius of the deformed sample. Meanwhile, there exist

$$R_\mathrm{f}=R_0\cdot\sqrt{\frac{h_0}{h_1}} \tag{4}$$

$$R_\mathrm{T}=\sqrt{3\frac{h_0}{h_1}R_0^2-2R_\mathrm{M}^2} \tag{5}$$

In actual operation, R_T can be averaged by measuring the top radius of the actual sample multiple times.

Based on the above equations, the true stress corrected by friction can be calculated.

The friction corrected stress−strain curve is represented by the dotted line in Fig. 2, from which it can be seen that the corrected stress is generally lower than the original stress. The corrected flow stress at the initial stage of deformation is not much different from the original flow stress. As the strain gradually increases, the stress increases. This is

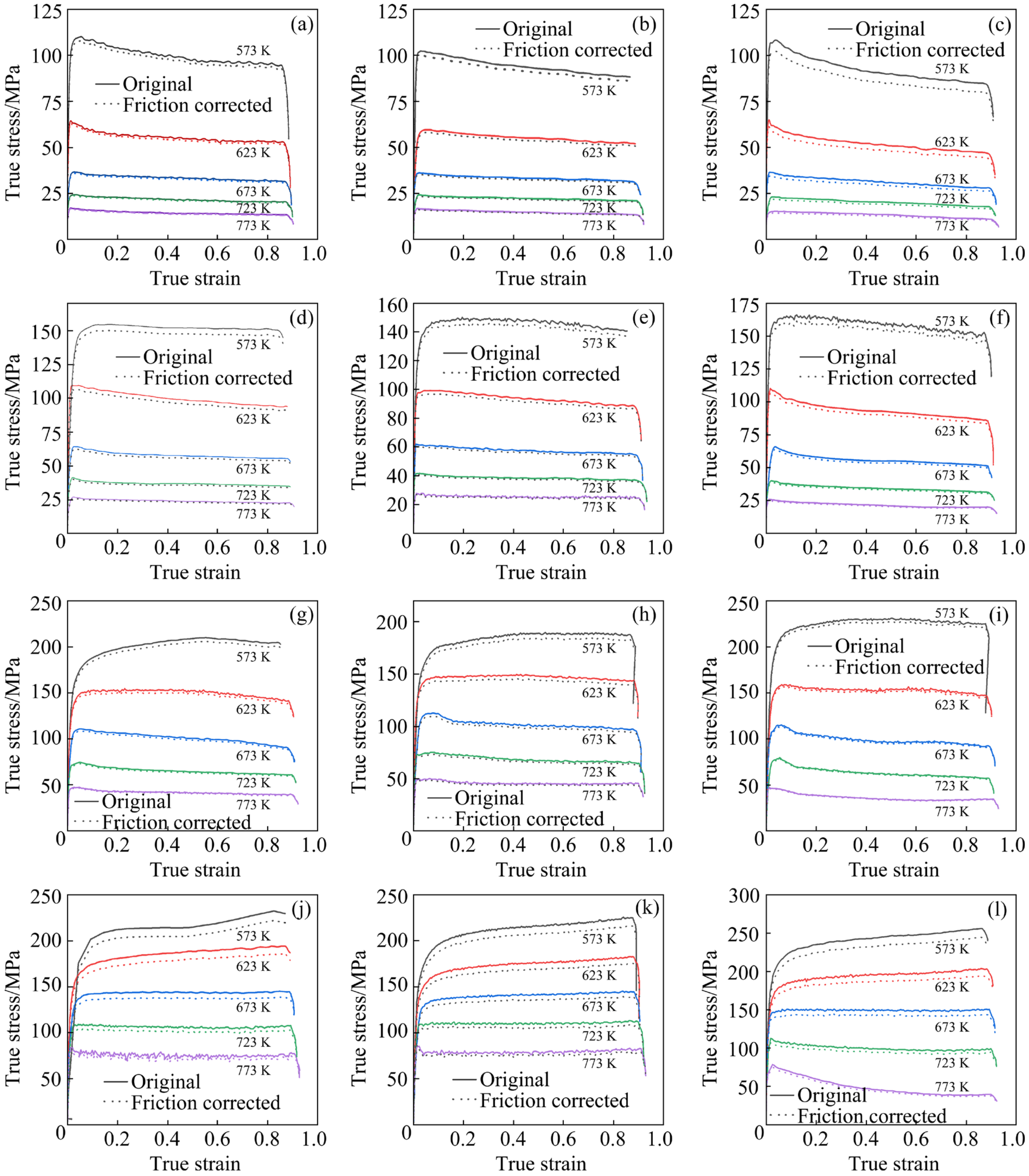

Fig. 2 Experimental and friction corrected flow stress−strain curves: (a, d, g, j) Al−6.00Mg alloy; (b, e, h, k) Al−6.00Mg−0.10Zr alloy; (c, f, i, l) Al−6.00Mg−0.25Sc−0.10Zr alloy; (a, b, c) 0.001 s^{-1}; (d, e, f) 0.01 s^{-1}; (g, h, i) 0.1 s^{-1}; (j, k, l) 1 s^{-1}

because the friction force increases by increasing the contact area between the specimen and container. Under different deformation temperatures and rates, the friction force is different. The lower the temperature is or the higher the strain rate is, the greater the friction force is. This can be attributed to the fact that the increase in temperature decreases the strength of the material, thus reducing the influence of friction.

3.2 Processing maps

The hot processing map based on the DMM can be used to characterize the relationship between the workability of alloys and the deformation conditions (temperature and strain rate) [17,18]. According to the DMM, the total dissipation (P) consists of the power dissipation (G) and dissipation energy (J) [13] at any time, which can be expressed as

$$P=\sigma\dot{\varepsilon}=G+J=\int_{0}^{\dot{\varepsilon}}\sigma\mathrm{d}\dot{\varepsilon}+\int_{0}^{\sigma}\dot{\varepsilon}\mathrm{d}\sigma \tag{6}$$

where G represents the power of plastic dissipation, J is related to the metallurgical mechanisms that dynamically occur to dissipate power, and $\dot{\varepsilon}$ is the strain rate. At a certain deformation temperature or strain, the relationship between the flow stress (σ) and the strain rate of alloys is

$$\sigma=K_{1}\dot{\varepsilon}^{m} \tag{7}$$

where m is the strain rate sensitivity index and K_1 is the material constant.

The distribution of energy dissipation depends on the strain rate sensitivity index m:

$$m=\left(\frac{\partial J}{\partial G}\right)_{\varepsilon,T}=\frac{\dot{\varepsilon}\mathrm{d}\sigma}{\sigma\mathrm{d}\dot{\varepsilon}}=\frac{\partial\lg\sigma}{\partial\lg\dot{\varepsilon}_{\varepsilon,T}} \tag{8}$$

$$J=\int_{0}^{\sigma}\dot{\varepsilon}\mathrm{d}\sigma=\frac{m\sigma\dot{\varepsilon}}{1+m} \tag{9}$$

For an ideal linear dissipator, when m=1, J reaches the maximum value ($J_{\max}=m\sigma/2$). In order to compare the dissipated energy, the DMM theory defines the power consumption efficiency factor η, which can be expressed as

$$\eta=\frac{J}{J_{\max}[2m/(m+1)]} \tag{10}$$

In the process of the deformation, power dissipation is sensitive to the deformation mechanism of the studied alloys. Therefore, the change of hot deformation mechanism of the studied alloy can be judged by the change of η. Studies show that when the η value is high, the alloy has two kinds of deformation: good deformation and unstable deformation. In order to eliminate the conditions of unstable deformation, PRASAD et al [17,18] established an instability criterion:

$$\xi(\dot{\varepsilon})=\frac{\partial\lg\left(\frac{m}{m+1}\right)}{\partial\lg\dot{\varepsilon}}+m<0 \tag{11}$$

where $\xi(\dot{\varepsilon})$ is flow instability parameter based on the Prasad's criterion.

The processing maps of the three alloys at the true strain of 0.9 are shown in Fig. 3. Domain 2 represents the instability regions ($\xi(\dot{\varepsilon})$<0), and the numbers on contours represent the efficiency of power dissipation in percentage. Obviously, at low deformation temperature and high strain rate, all three alloys are in unstable regions. The maximum processing efficiencies of Al−6.00Mg, Al−6.00Mg−0.10Zr and Al−6.00Mg−0.25Sc−0.10Zr alloys are 46.60%, 45.60%, and 50%, respectively. It is well known that the optimal hot deformation process parameters should be selected in the safe and high-power dissipation domain [19,20]. According

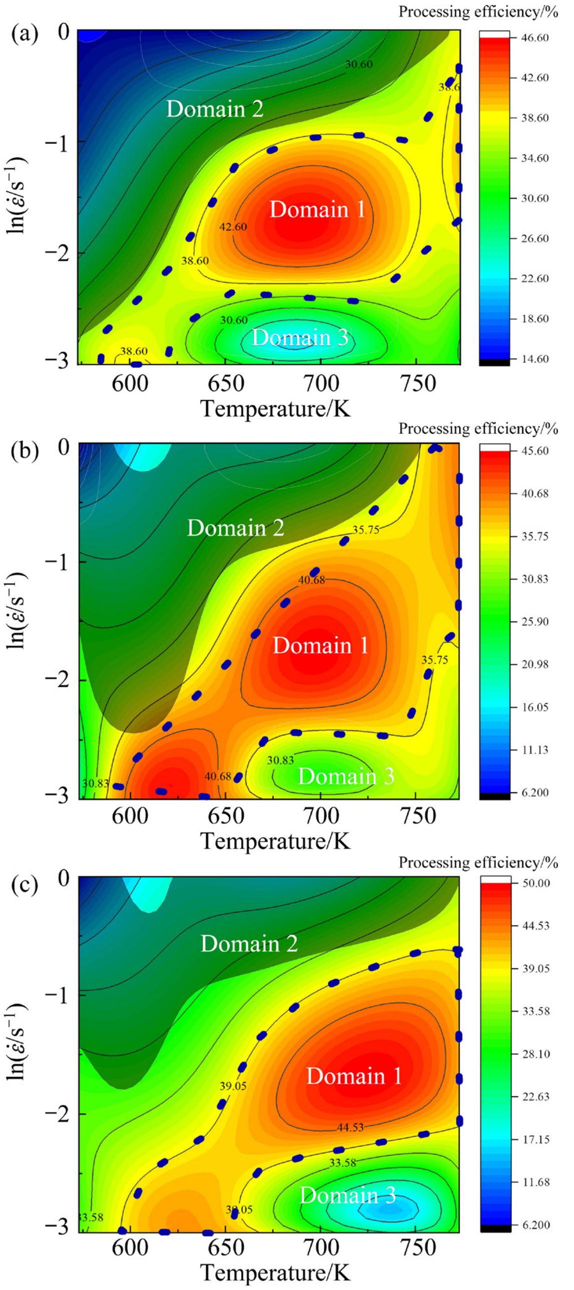

Fig. 3 Processing maps at true strain of 0.9: (a) Al−6.00Mg alloy; (b) Al−6.00Mg−0.10Zr alloy; (c) Al−6.00Mg−0.25Sc−0.10Zr alloy

to the processing maps of the three alloys, Domain 2 of the Al−Mg alloy is the largest, and the unsafe zone (Domain 1) of the Al−Mg alloy containing Sc and Zr is the largest.

It has been reported that when the processing efficiency is greater than 30%, the deformation mechanism is considered as DRX. In this condition the alloys have good workability [21]. The Al−6.00Mg alloy has the most efficient process parameter in the temperature range of 630−725 K and the strain rate range of 0.005−0.06 s^{-1}. While, the Al−6.00Mg−0.10Zr alloy has the most efficient process parameter in the temperature range of 650−725 K and the strain rate range of 0.006−0.05 s^{-1}. For the Al−6.00Mg−0.25Sc−0.10Zr alloy, the corresponding temperature and strain rate range are respectively 675−760 K and 0.006−0.05 s^{-1}. Besides, the processing maps of the three alloys can be divided into three domains, which are the unsafe domain (Domain 1), efficient domain (Domain 2) and inefficient domain (Domain 3). The microstructure evolution in these three domains will be investigated, and the deformation mechanism will be discussed.

3.3 Microstructural features of deformed alloys

Figures 4−6 are IPF maps of Al−6.00Mg, Al−6.00Mg−0.10Zr and Al−6.00Mg−0.25Sc−0.10Zr alloys, respectively, under different deformation conditions (573 K, 0.1 s^{-1}; 573 K, 0.01 s^{-1}; 673 K,

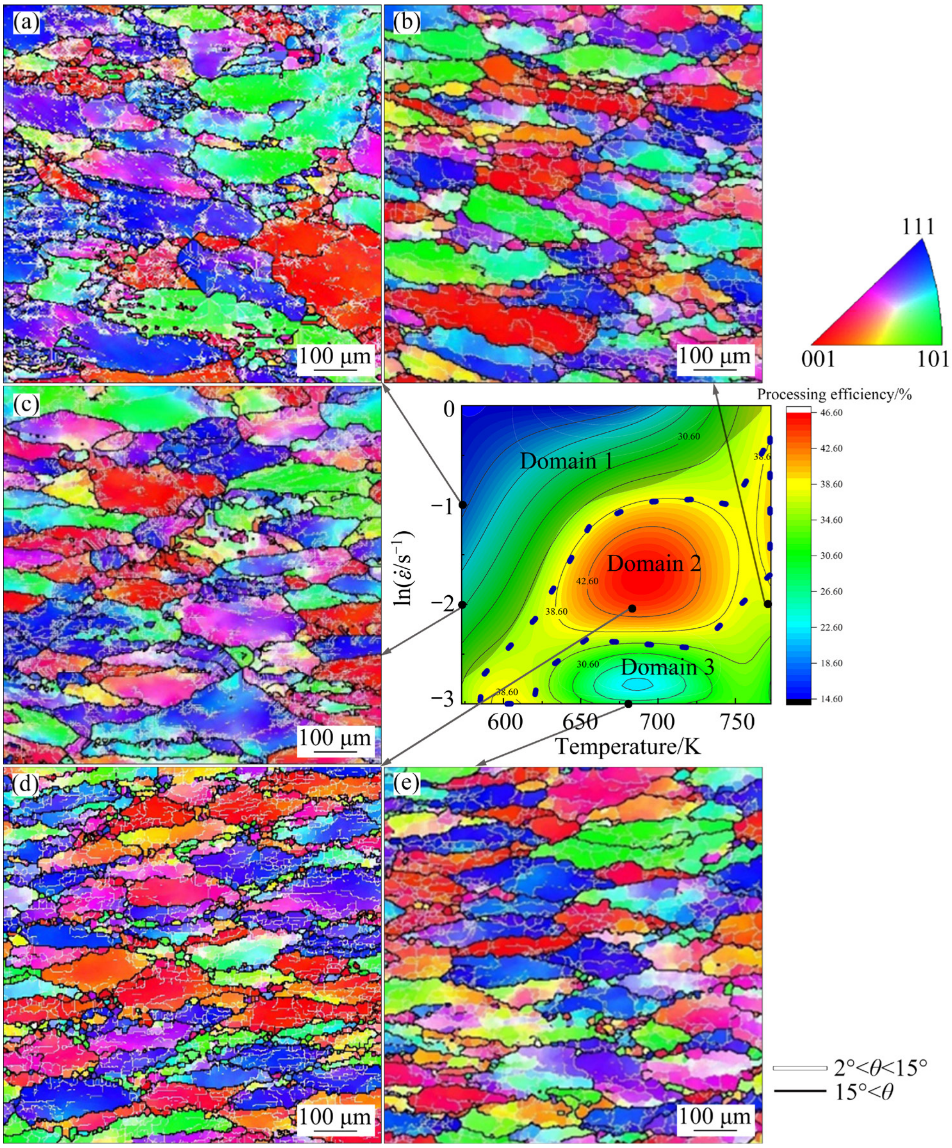

Fig. 4 IPF maps of Al−6.00Mg alloy under different hot deformation conditions (LAGBs (2°−15°) are in white and HAGBs (>15°) are in black): (a) 573 K, 0.1 s^{-1}; (b) 773 K, 0.01 s^{-1}; (c) 573 K, 0.01 s^{-1}; (d) 673 K, 0.01 s^{-1}; (e) 673 K, 0.001 s^{-1}

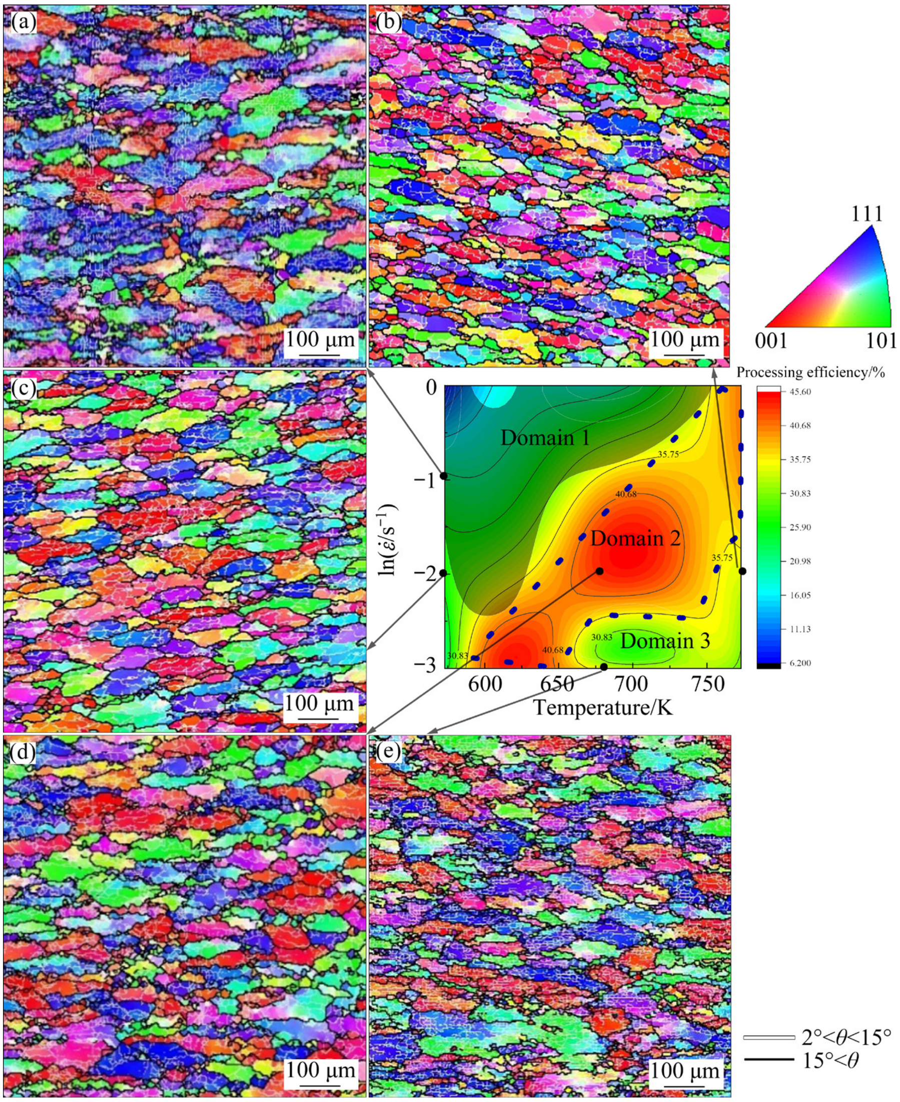

Fig. 5 IPF maps of Al−6.00Mg−0.10Zr alloy under different hot deformation conditions (LAGBs (2°−15°) are in white and HAGBs (>15°) are in black): (a) 573 K, 0.1 s^{-1}; (b) 773 K, 0.01 s^{-1}; (c) 573 K, 0.01 s^{-1}; (d) 673 K, 0.01 s^{-1}; (e) 673 K, 0.001 s^{-1}

0.01 s^{-1}; 673 K, 0.001 s^{-1}; 773 K, 0.01 s^{-1}). After deformation, the initial grains are elongated perpendicularly to the compression direction. At the same time, some low angle grain boundaries (LAGBs) are formed inside the deformed grains [22]. It can be seen from Fig. 7 that the proportion of LAGBs is larger than that of the high angle grain boundaries (HAGBs) in the three alloys. As the initial grains are equiaxed, the generated substructure with LAGBs can be considered as DRV, and the new grain with HAGBs can be considered as DRX [23,24].

By comparing the microstructure of the three alloys, it can be found that when Zr or Sc+Zr is added to the Al−Mg alloy, the fraction of LAGBs significantly increases, which means that DRX is suppressed. For Domain 1 (673 K, 0.01 s^{-1}) in the processing maps of the three alloys, the fine DRX grains are formed along the initial grain boundaries. At the low deformation temperature or the high strain rate (573 K, 0.01 s^{-1}; 573 K, 0.1 s^{-1}) in Domain 2, the degree of deformation is much higher. Due to the higher deformation temperature and more sufficient deformation time, the fraction of LAGB decreases and the DRX grain size increases in Domain 3.

3.4 Dislocation density

In order to characterize the dislocation density of Domain 1 (673 K, 0.01 s^{-1}), the modified

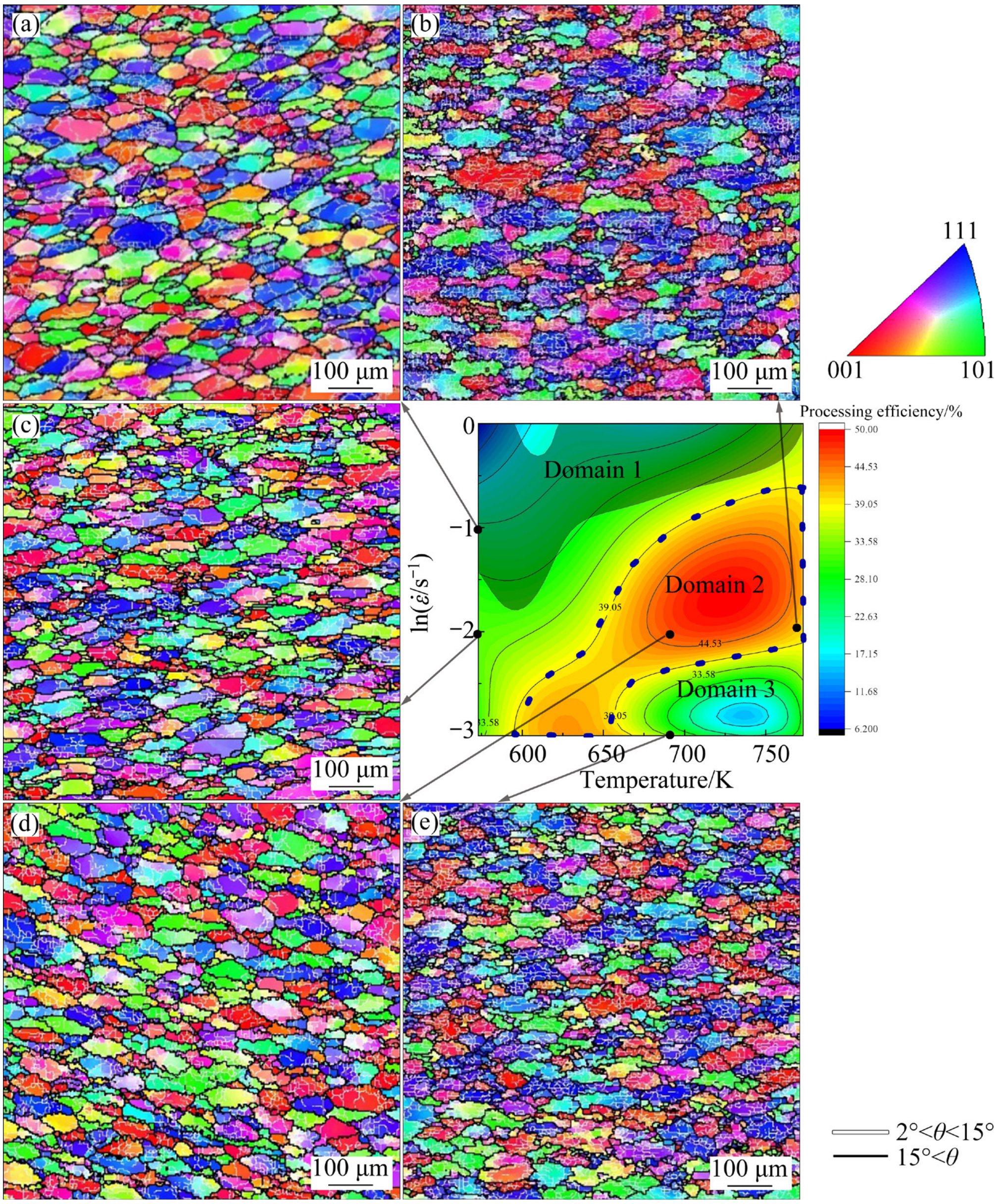

Fig. 6 IPF maps of Al−6.00Mg−0.25Sc−0.10Zr alloy under different hot deformation conditions (LAGBs (2°−15°) are in white and HAGBs (>15°) are in black): (a) 573 K, 0.1 s^{-1}; (b) 773 K, 0.01 s^{-1}; (c) 573 K, 0.01 s^{-1}; (d) 673 K, 0.01 s^{-1}; (e) 673 K, 0.001 s^{-1}

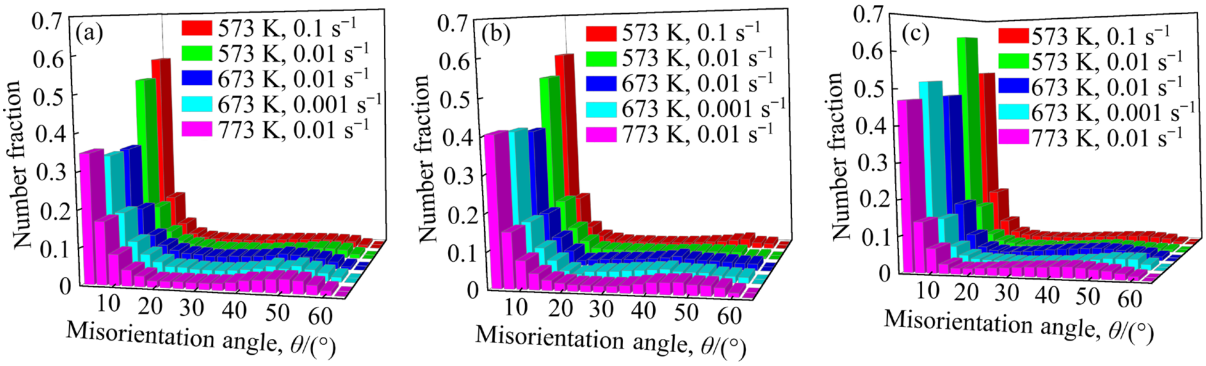

Fig. 7 Misorientation angles of three alloys under different hot deformation conditions: (a) Al−6.00Mg; (b) Al−6.00Mg−0.10Zr; (c) Al−6.00Mg−0.25Sc−0.10Zr

Williamson−Hall equation was used to fit the full width at half maximum (FWHM) [25]. The Williamson−Hall equation reveals that different dislocation densities are related to different FWHMs. In this way, the dislocation density of the sample can be calculated. According to the modified Williamson−Hall equation, as shown in Eq. (12), the FWHM is used for liner fitting. Then, the dislocation density can be calculated by the slope of the fitted curve.

$$\frac{\beta\cos\theta}{\lambda}\approx\frac{\gamma}{D}+\left(\frac{\pi M^2 b^2}{2}\right)^{1/2}\rho^{1/2}KC^{1/2}+O(K^2C) \tag{12}$$

where θ is the Bragg's angle, λ(=0.154046 nm) is the wavelength, β is the FWHM of the diffraction peak. D, b and ρ are the size of the coherent scattering domain, the amplitude of the Burgers vector of dislocations (b=0.286 nm for aluminum alloy) and the dislocation density, respectively. γ(=0.9) is the shap factor of the corresponding peak. M is the dislocation arrangement parameter (M=1−2) [25,26]. K is the modulus of the diffraction vector, and the value is 2sin θ/λ. $O(K^2C)$ stands for higher-order term residues. C represents the contrast factor of dislocation. For cubic polycrystalline materials, the contrast factor can be obtained by the fourth-order polynomial of the Miller index by Eq. (13) [26]:

$$C=C_{h00}(1-qH_1^2) \tag{13}$$

where C_{h00} is the average contrast factor of the h00 reflections; q depends on the proportions of edge and screw dislocations, and on the elastic constants of the investigated material. The expression of H_1 is shown in Eq. (14) [27]:

$$H_1^2=(h^2k^2+k^2l^2+h^2l^2)/(h^2+k^2+l^2)^2 \tag{14}$$

where h, k and l are indices of crystal face.

Formula (12) is applicable to the three alloys. $(\beta\cos\theta)/\lambda$ and $KC^{1/2}$ are different for the three alloys.

The XRD results and the linear fits of the Williamson−Hall equations of Domain 1 (673 K, 0.01 s^{-1}) in the three alloys are shown in Fig. 8. The calculated dislocation densities of Domain 1 (673 K, 0.01 s^{-1}) in the three alloys are 2.68×10^{16}, 8.93×10^{16}, and 6.1×10^{17} m^{-2}, respectively. Thus, it is obvious that adding Zr/(Sc+Zr) to the Al−Mg alloy increases the dislocation density of the alloy during the hot deformation process.

4 Discussion

4.1 Effects of Zr or Sc+Zr addition on dynamic recrystallization during deformation

The grain orientation spread (GOS) map can be used to quickly identify the recrystallized grains of the deformed samples. The general consensus is that when the GOS of a grain is smaller than 2° it can be considered that dynamic recrystallization will occur in the grain [28]. If the misorientation angle between two grains is 15°, then the grains with GOS<2° are DRX grains. Figure 9 shows the GOS maps of the three alloys under different deformation conditions. The area of GOS<2° is indicated by colors, and that of GOS>2° is indicated by white. HAGBs and LAGBs are marked as black and grey lines on the map, respectively. The colored regions in these figures represent DRX grains.

The variation of the dynamic recrystallized fraction of grains under different deformation

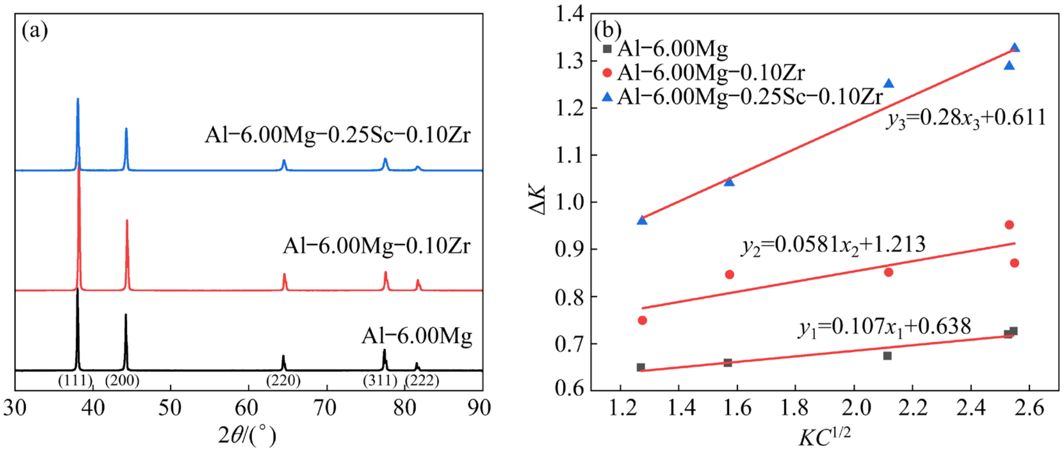

Fig. 8 XRD pattern (a) and liner fitting of modified Williamson−Hall equation (b)

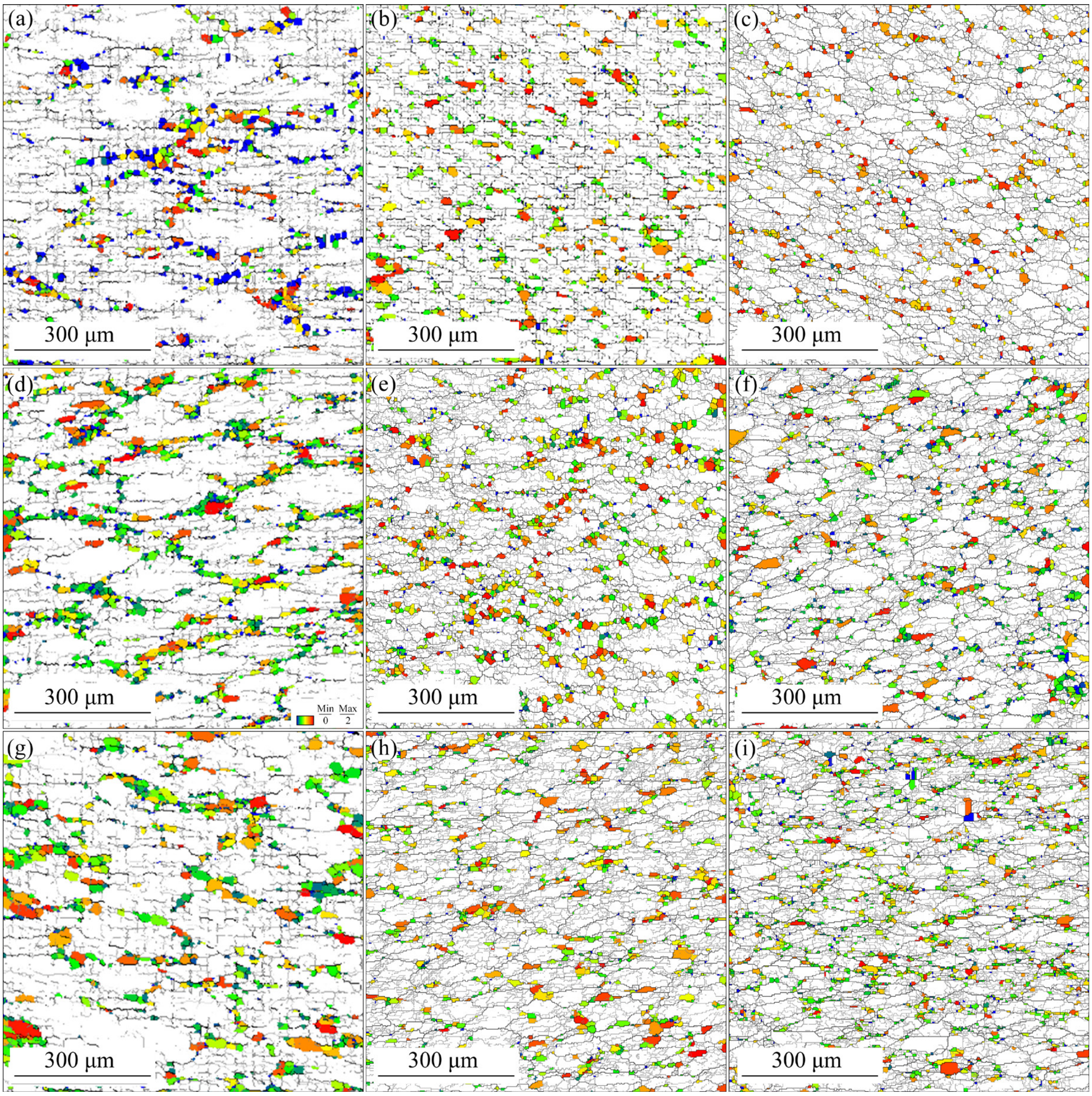

Fig. 9 GOS maps of three alloys under different hot deformation conditions: (a, d, g) Al−6.00Mg; (b, e, h) Al−6.00Mg−0.10Zr; (c, f, i) Al−6.00Mg−0.25Sc−0.10Zr; (a, b, c) 573 K, 0.01 s^{-1}; (d, e, f) 673 K, 0.01 s^{-1}; (g, h, i) 773 K, 0.01 s^{-1} (LAGBs (2°−15°) are in white and HAGBs (>15°) are in black)

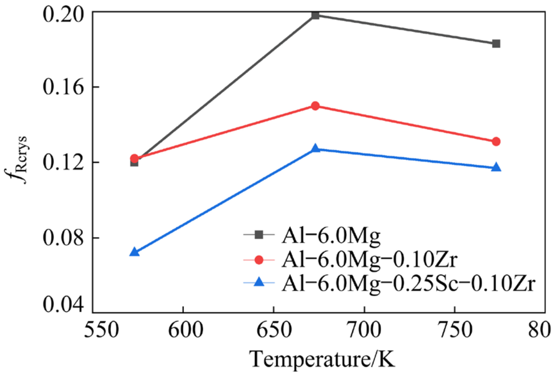

Fig. 10 Variation of fraction of recrystallized grains (f_{Rcrys}) (obtained from GOS<2° and grain to grain misorientation set to be 15°)

conditions (573 K, 0.01 s^{-1}; 673 K, 0.01 s^{-1}; 773 K, 0.01 s^{-1}) is shown in Fig. 10. By combining the results of Fig. 9, it can be found that the DRX grain size and the ratio of the samples deformed at high temperatures are larger than those of the samples deformed at low temperatures. The DRX grain ratio reaches a maximum at 673 K. Besides, it can be found that the Al−Mg alloy has the largest dynamic recrystallization fraction, and the Al−6.00Mg−0.25Sc−0.10Zr alloy has the smallest one. The above results show that the addition of Zr or Sc+Zr can hinder the occurrence of dynamic recrystallization.

4.2 Effects of Zr or Sc+Zr addition on dislocation accumulation during deformation

The kernel average misorientation (KAM) maps of the three alloys under different deformation conditions (573 K, 0.01 s^{-1}; 673 K, 0.01 s^{-1}; 773 K, 0.01 s^{-1}) are shown in Fig.11. The KAM map can be utilized to visualize the strain position in the deformed sample. The red area represents the area with high KAM. In this area, the dislocation accumulation is high. In contrast, the blue area represents area with low KAM, in which, the dislocation is recovered [29,30]. It can be seen from Fig. 11 that the dislocation accumulation of the three alloys is high at a low temperature of 573 K. The areas with high KAM values of the three alloys all locate near grain boundaries. This is why the recrystallized grains grow along the grain boundaries.

After being deformed at 673 K and 0.01 s^{-1}, the stored energy in the grains is very low. In Domain 1 of the processing map, the processing efficiency of the three alloys is the highest at 673 K and 0.01 s^{-1}. It is worth mentioning that when the processing temperature of the Al−6.00Mg−0.25Sc−0.10Zr alloy is 773 K, there is still a large amount of dislocation accumulation inside the grains. Combined with the processing map, the Al−6.00Mg−0.25Sc−0.10Zr alloy is in the instability zone when the deformation condition is 773 K, 1 s^{-1}. This means that the strain storage energy is very high at high temperatures and high strain rates. Therefore, there is not enough time for the occurrence of dynamic recrystallization and instability.

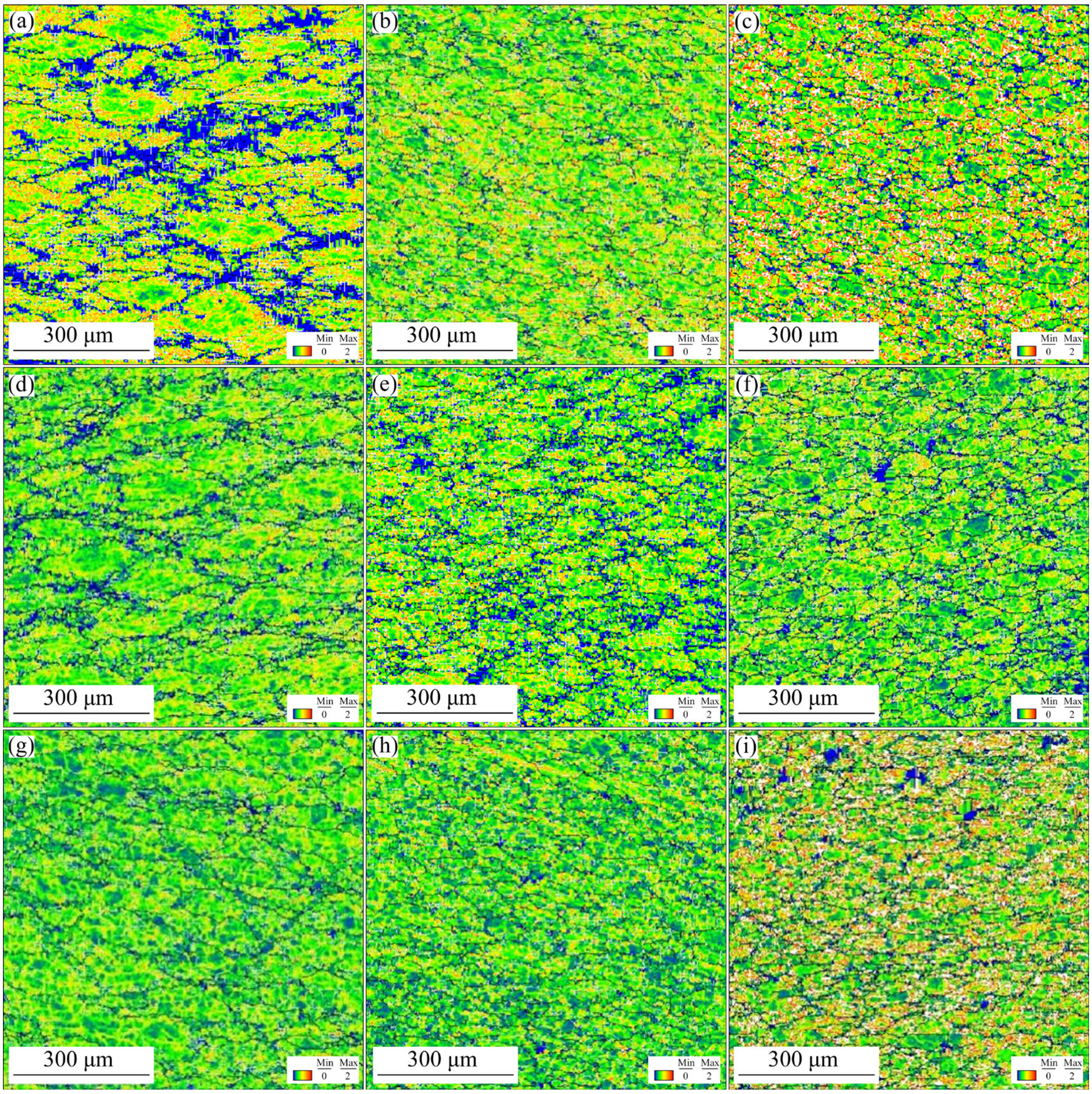

Fig. 11 KAM maps of three alloys under different hot deformation conditions: (a, d, g) Al−6.00Mg; (b, e, h) Al−6.00Mg−0.10Zr; (c, f, i) Al−6.00Mg−0.25Sc−0.10Zr; (a, b, c) 573 K, 0.01 s^{-1}; (d, e, f) 673 K, 0.01 s^{-1}; (g, h, i) 773 K, 0.01 s^{-1} (LAGBs (2°−15°) are in white and HAGBs (>15°) are in black)

4.3 Effects of Zr or Sc+Zr addition on hot workability

As mentioned above, DRX is a process driven by the deformation stored energy. Initially, as the deformation increases, the energy stored in grains increases due to the dislocation accumulation. A critical strain is required to store a sufficient energy in the grains until it can trigger DRX. The stored energy distribution in the grains can be described by the grain reference orientation deviation (GROD) map which reflects the location of strain. Figure 12 shows the GROD maps of the studied alloys under different deformation conditions (573 K, 0.01 s^{-1}; 673 K, 0.01 s^{-1}; 773 K, 0.01 s^{-1}). It can be observed from the figure that the maximum GROD values of Al−6.00Mg and Al−6.00Mg−0.10Zr alloys decrease with the increase of the deformation temperature. This means that Al−6.00Mg and Al−6.00Mg−0.10Zr alloys are safer to deform at high temperatures than at low temperatures. However, the GROD value of Al−6.00Mg−0.25Sc−0.10Zr alloy at 773 K is higher than that at 673 K. This means that the strain energy after high temperature deformation is high in the Al−6.00Mg−0.25Sc−0.10Zr alloy. High strain energy will easily lead to cracking during deformation.

Besides, there is not much difference in the peak GROD value of the Al−Mg alloy under different deformation conditions. After adding Zr or Sc+Zr to the Al−Mg alloy, the GROD peak values increase, indicating that the strain energy stored in the grain increases.

Figures 13(a)−(c) show morphologies of the three alloys under different deformation conditions.

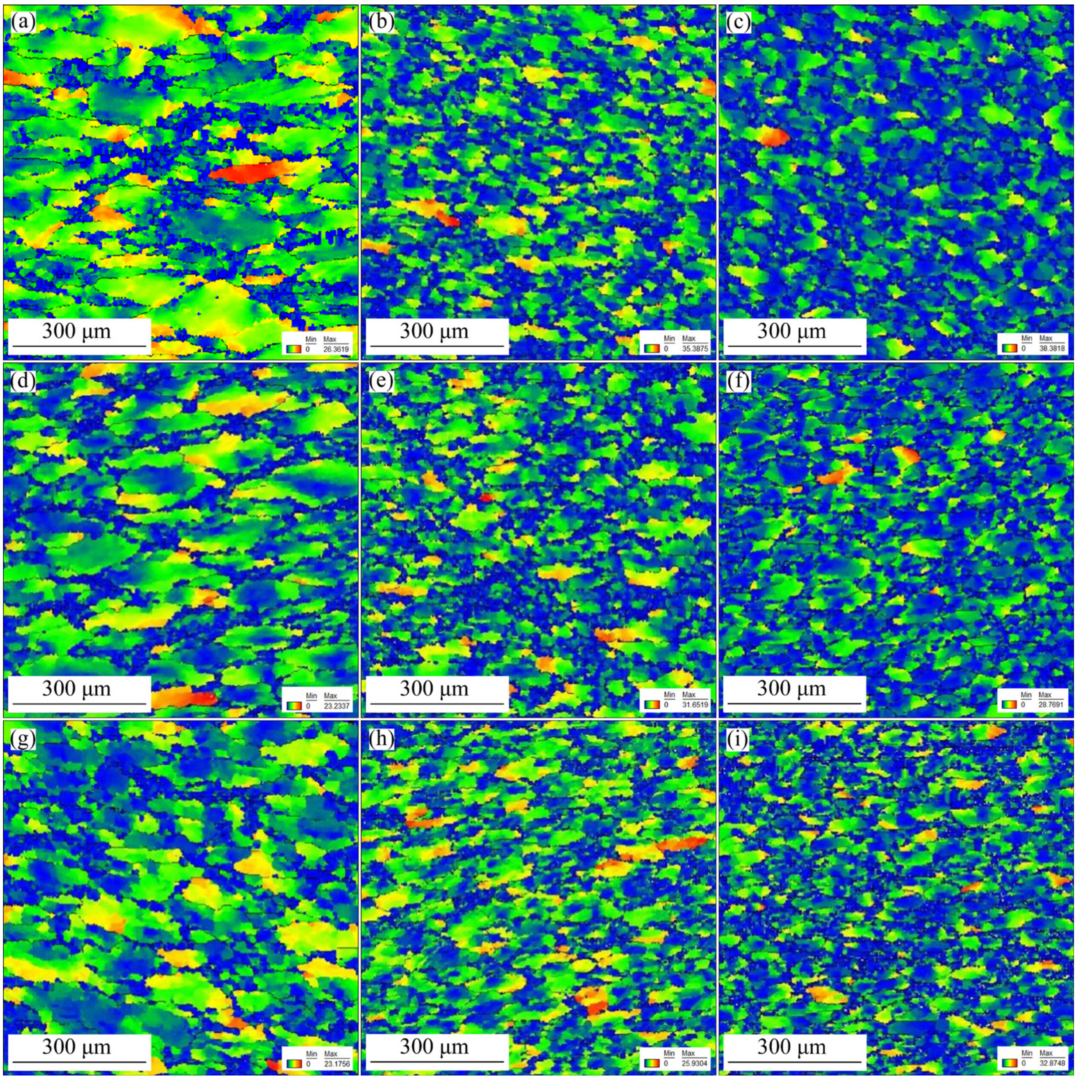

Fig. 12 GROD maps of three alloys under different hot deformation conditions: (a, d, g) Al−6.00Mg; (b, e, h) Al−6.00Mg−0.10Zr; (c, f, i) Al−6.00Mg−0.25Sc−0.10Zr; (a, b, c) 573 K, 0.01 s^{-1}; (d, e, f) 673 K, 0.01 s^{-1}; (g, h, i) 773 K, 0.01 s^{-1} (LAGBs (2°−15°) are in white and HAGBs (>15°) are in black)

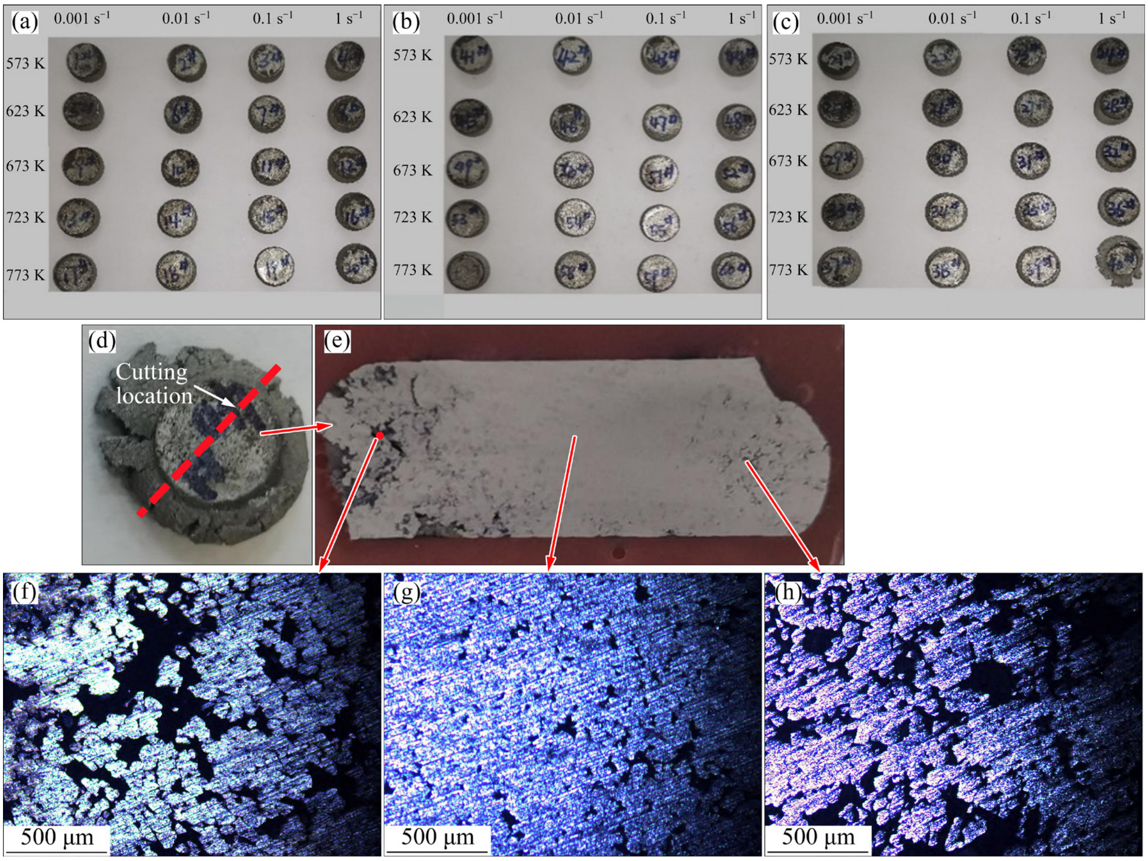

Fig. 13 Morphologies of three alloys after hot compression deformation (Three alloy samples were deformed at temperatures ranging from 573 to 773 K and strain rates ranging from 0.001 to 1 s^{-1}): (a) Al−6.00Mg; (b) Al−Mg−0.10Zr; (c) Al−6.00Mg−0.25Sc−0.10Zr; (d) Magnified image of cracked samples (Al−6.00Mg−0.25Sc−0.10Zr, 773 K and 1 s^{-1}); (e) OM macrophotograph of sample in (d); (f, g, h) Magnified OM images of sample in (d)

It can be seen that only the Al−6.00Mg−0.25Sc−0.10Zr alloy has obvious cracking when the hot deformation state is 773 K and 1 s^{-1}. Figures 13(d) shows the morphology of the Al−6.00Mg−0.25Sc−0.10Zr alloy under the hot deformation condition of 773 K and 1 s^{-1}. Figure 13(e) represents the side section diagram of the sample perpendicular to the compression direction. Figures 13(f)−(h) show the metallographic micrograph of the sample. It can be clearly seen that there are obvious cracks in the sample, and the cracks are mainly located at the edges of the sample, with fewer cracks in the middle of the sample. Meanwhile, the cracks originate from the sample edges and gradually extend to the middle. The addition of Zr or Sc+Zr increases the dislocation density and strain energy inside the grain of the Al−Mg alloys during hot deformation. But it reduces the recrystallization fraction. Therefore, the work hardening effect is enhanced and the true stress is increased after adding Zr or Sc+Zr to the Al−Mg alloys.

5 Conclusions

(1) The addition of Zr or Sc+Zr reduces the range of unstable regions in the Al−Mg alloys according to processing map, which improves the hot workability of the studied Al−Mg alloys.

(2) The addition of Zr or Sc+Zr increases the dislocation density of the Al−Mg alloys during the hot deformation. The dislocation densities of Al−6.00Mg, Al−6.00Mg−0.10Zr and Al−6.00Mg−0.25Sc−0.10Zr alloys under the deformation conditions of 673 K and 0.01 s^{-1} are 2.68×10^{16}, 8.93×10^{16}, and 6.1×10^{17} m^{-2}, respectively.

(3) The addition of Zr or Sc+Zr can inhibit the dynamic recrystallization of the Al−Mg alloys and increase the dislocation accumulation in grains during hot deformation.

(4) The Al−6.00Mg−0.25Sc−0.10Zr alloy cracks due to the extensive accumulation of dislocations in the grains when the hot deformation

condition is 773 K and 1 s^{-1}.

(5) The addition of Zr or Sc+Zr increases the dislocation density and strain energy inside the grain of the Al−Mg alloys during hot deformation. But it reduces the recrystallization fraction.

Acknowledgments

The authors are grateful for the financial supports from the Natural Science Foundation of Hunan Province, China (Nos. 2020JJ4114, 2016JJ3151), the National Natural Science Foundation of China (No. 51601229), the Young Elite Scientist Sponsorship Program by CAST, China (No. 2015QNRC001), the Hunan Province Innovation Platform and Talent Plan Project, China (No. 2015RS4001), and the Open-end Fund for the Valuable and Precision Instruments of Central South University, China (No. CSUZC201815).

References

[1] SAUVAGE X, ENIKEEV N, VALIEV R, VALIEV Y, NASEDKINA Y, MURASHKIN M. Atomic-scale analysis of the segregation and precipitation mechanisms in a severely deformed Al−Mg alloy [J]. Acta Materialia, 2014, 72: 125−136.

[2] ZHAO Y F, POLYAKOV M N, MECKLENBURG M, KASSNER M E, HODGE A M. The role of grain boundary plane orientation in the β phase precipitation of an Al−Mg alloy [J]. Scripta Materialia, 2014, 89: 49−52.

[3] LIU Y, LIU M P, CHEN X F, CAO Y, ROVEN H J, MURASHKIN M, VALIEV R Z, ZHOU H. Effect of Mg on microstructure and mechanical properties of Al−Mg alloys produced by high pressure torsion [J]. Scripta Materialia, 2019, 159: 137−141.

[4] LIU T W, WANG Q D, TANG H P, LI Z Y, LEI C, EBRAHIMI M, JIANG H Y, DING W J. Microstructure and mechanical properties of squeeze-cast Al−5.0Mg−3.0Zn−1.0Cu alloys in solution-treated and aged conditions [J]. Transactions of Nonferrous Metals Society of China, 2020, 30(9): 2326−2338.

[5] BABANIARIS S, RAMAJAYAM M, JIANG L, VARMA R, LANGAN T, DORIN T. Effect of $Al_3(Sc,Zr)$ dispersoids on the hot deformation behaviour of 6xxx-series alloys: A physically based constitutive model [J]. Materials Science and Engineering: A, 2020, 793: 139873.

[6] XIAO Q F, HUANG J W, JIANG F Q, WU Y F, XU G F. Effects of minor Sc and Zr additions on mechanical properties and microstructure evolution of Al−Zn−Mg−Cu alloys [J]. Transactions of Nonferrous Metals Society of China, 2020, 30(6): 1429−1438.

[7] JIANG J Y, JIANG F, HUANG H F, ZHANG M H, TANG Z Q, TONG M M. Hot deformation analysis and microstructure evolution of Al−Mg−Mn−Sc−Zr alloy by isothermal compression [J]. Journal of Alloys and Compounds, 2021, 858: 157655.

[8] YANG Q B, DENG Y J, YANG M, ZHANG Z Q, LI W G, LIU Q. Effect of Al_3Zr particles on hot-compression behavior and processing map for Al−Cu−Li based alloys at elevated temperatures [J]. Transactions of Nonferrous Metals Society of China, 2020, 30(4): 872−882.

[9] MOMENI A, DEHGHANI K. Hot working behavior of 2205 austenite–ferrite duplex stainless steel characterized by constitutive equations and processing maps [J]. Materials Science and Engineering: A, 2011, 528(3): 1448−1454.

[10] XIA Y F, JIANG W, CHENG Q, JIANG L, JIN L. Hot deformation behavior of Ti−6Al−4V−0.1Ru alloy during isothermal compression [J]. Transactions of Nonferrous Metals Society of China, 2020, 30(1): 134−146.

[11] LUO J, LI M Q, WU B. The correlation between flow behavior and microstructural evolution of 7050 aluminum alloy [J]. Materials Science and Engineering: A, 2011, 530: 559−564.

[12] CAO F R, YIN B, LIU S Y, SHI L, WANG S C, WEN J L. Microstructural evolution, flow stress and constitutive modeling of Al−1.88Mg−0.18Sc−0.084Er alloy during hot compression [J]. Transactions of Nonferrous Metals Society of China, 2021, 31(1): 53−73.

[13] ZANG Q H, YU H S, LEE Y S, KIM M S, KIM M S, KIM H W. Hot deformation behavior and microstructure evolution of annealed Al−7.9Zn−2.7Mg−2.0Cu (wt.%) alloy [J]. Journal of Alloys and Compounds, 2018, 763: 25−33.

[14] LIN X J, HUANG H J, YUAN X G, WANG Y X, ZHENG B W, ZUO X J, ZHOU G. Study on hot deformation behavior and processing map of a Ti−47.5Al−2.5V− 1.0Cr−0.2Zr alloy with a fully lamellar microstructure [J]. Journal of Alloys and Compounds, 2022, 901: 163648.

[15] EBRAHIMI R, NAJAFIZADEH A. A new method for evaluation of friction in bulk metal forming [J]. Journal of Materials Processing Technology, 2004, 152(2): 136−143.

[16] LIANG X P, LIU Y, LI H Z, ZHOU C X, XU G F. Constitutive relationship for high temperature deformation of powder metallurgy Ti−47Al−2Cr−2Nb−0.2W alloy [J]. Materials & Design, 2012, 37: 40−47.

[17] PRASAD Y V R K, GEGEL H L, DORAIVELU S M, MALAS J C, MORGAN J T, LARK K A, BARKER D R. Modeling of dynamic material behavior in hot deformation: Forging of Ti-6242 [J]. Metallurgical Transactions A, 1984, 15(10): 1883−1892.

[18] PRASAD Y V R K, SESHACHARYULU T. Processing maps for hot working of titanium alloys [J]. Materials Science and Engineering: A, 1998, 243(1): 82−88.

[19] WANG S, HOU L G, LUO J R, ZHANG J S, ZHUANG L Z. Characterization of hot workability in AA 7050 aluminum alloy using activation energy and 3-D processing map [J]. Journal of Materials Processing Technology, 2015, 225: 110−121.

[20] WU Y T, LIU Y C, LI C, XIA X C, HUANG Y, LI H, WANG H P. Deformation behavior and processing maps of Ni_3Al-based superalloy during isothermal hot compression [J]. Journal of Alloys and Compounds, 2017, 712: 687−695.

[21] YAN J, PAN Q L, LI B, HUANG Z Q, LIU Z M, YIN Z M. Research on the hot deformation behavior of Al−6.2Zn−0.70Mg−0.3Mn−0.17Zr alloy using processing map [J]. Journal of Alloys and Compounds, 2015, 632: 549−557.

[22] MOGHADDAM M, ZAREI-HANZAKI A, PISHBIN M H, SHAFIEIZAD A H, OLIVEIRA V B. Characterization of the microstructure, texture and mechanical properties of 7075 aluminum alloy in early stage of severe plastic deformation [J]. Materials Characterization, 2016, 119: 137−147.

[23] BRANDON D G. The structure of high-angle grain boundaries [J]. Acta Metallurgica, 1966, 14(11): 1479−1484.

[24] ZHAO J H, DENG Y L, TANG J G, ZHANG J. Influence of strain rate on hot deformation behavior and recrystallization behavior under isothermal compression of Al−Zn−Mg−Cu alloy [J]. Journal of Alloys and Compounds, 2019, 809: 151788.

[25] WILKENS M. In fundamental aspects of dislocation theory [M]. 2nd ed. Washington: National Bureau of Standards Special Publication, 1970.

[26] UNGAR T, GUBICZA J, RIBARIK G, BORBELY A. Crystallite size distribution and dislocation structure determined by diffraction profile analysis: Principles and practical application to cubic and hexagonal crystals [J]. Journal of Applied Crystallography, 2001, 34(3): 298−310.

[27] UNGAR T, DRAGOMIR I, REVESZ A, BORBELY A. The contrast factors of dislocations in cubic crystals: The dislocation model of strain anisotropy in practice [J]. Journal of Applied Crystallography, 1999, 32(5): 992−1002.

[28] KAPOOR R, REDDY G B, SARKAR A. Discontinuous dynamic recrystallization in α-Zr [J]. Materials Science and Engineering: A, 2018, 718: 104−110.

[29] ZHONG Y, YIN F, SAKAGUCHI T, NAGAI K, YANG K. Dislocation structure evolution and characterization in the compression deformed Mn–Cu alloy [J]. Acta Materialia, 2007, 55(8): 2747−2756.

[30] GURAO N P, SUWAS S. Deformation behaviour at macro- and nano-length scales: The development of orientation gradients [J]. Materials Letters, 2013, 99: 81−85.

Zr/(Sc+Zr)微合金化对 Al−Mg 合金在热压缩变形中动态再结晶、位错密度和热加工性能的影响

邓英[1,2]，朱鑫文[1]，赖毅[1]，郭一帆[1]，傅乐[1,3]，徐国富[1,2]，黄继武[1,2]

1. 中南大学 材料科学与工程学院，长沙 410083；
2. 中南大学 有色金属材料科学与工程湖南省重点实验室，长沙 410083；
3. Applied Materials Science, Department of Engineering Science, Uppsala University, Uppsala, 75121, Sweden

摘　要：采用热压缩试验和电子显微分析方法研究 Al−6.00Mg、Al−6.00Mg−0.10Zr 和 Al−6.00Mg−0.25Sc−0.10Zr (质量分数，%)合金的变形行为和显微组织特征。结果表明，在最大加工效率条件(673 K，0.01 s^{-1})下变形时，Al−6.00Mg、Al−6.00Mg−0.10Zr 和 Al−6.00Mg−0.25Sc−0.10Zr 合金的位错密度分别为 2.68×10^{16}、8.93×10^{16} 和 6.1×10^{17} m^{-2}；其动态再结晶分数分别为 19.8%、15.0%和 12.7%。中心点平均取向差(KAM)分析表明，通过添加 Zr 或 Sc+Zr，Al−Mg 合金晶界附近的位错密度增加。此外，基于动态材料模型(DMM)建立的热加工图表明，添加 Zr 或 Sc+Zr 能减小 Al−Mg 合金的低温不稳定域的范围，但会增大高温和高应变不稳定域的范围。实验结果进一步证明，在变形条件下，仅 Al−6.00Mg−0.25Sc−0.10Zr 合金在 773 K 和 1 s^{-1} 时开裂。

关键词：Al−Mg 合金；Sc；Zr；热变形；位错密度；动态再结晶

(Edited by Wei-ping CHEN)